The South Pacific Meridional Mode as a Thermally Driven Source of ENSO Amplitude Modulation and Uncertainty

SARAH M. LARSON

Atmospheric and Oceanic Sciences Department, and Nelson Institute Center for Climatic Research, University of Wisconsin–Madison, Madison, Wisconsin

KATHY V. PEGION

Department of Atmospheric, Oceanic, and Earth Sciences, George Mason University, Fairfax, Virginia

BEN P. KIRTMAN

Rosenstiel School of Marine and Atmospheric Science, University of Miami, Miami, Florida

(Manuscript received 23 October 2017, in final form 9 March 2018)

ABSTRACT

This study seeks to identify thermally driven sources of ENSO amplitude and uncertainty, as they are relatively unexplored compared to wind-driven sources. Pacific meridional modes are argued to be wind triggers for ENSO events. This study offers an alternative role for the South Pacific meridional mode (SPMM) in ENSO dynamics, not as an ENSO trigger, but as a coincident source of latent heat flux (LHF) forcing of ENSO SSTA that, if correctly (incorrectly) predicted, could reduce (increase) ENSO prediction errors. We utilize a coupled model simulation in which ENSO variability is perfectly periodic and each El Niño experiences identical wind stress forcing. Differences in El Niño amplitude are primarily thermally driven via the SPMM. When El Niño occurs coincidentally with positive phase SPMM, the positive SPMM LHF anomaly counteracts a fraction of the LHF damping of El Niño, allowing for a more intense El Niño. If the SPMM phase is instead negative, the SPMM LHF amplifies the LHF damping of El Niño, reducing the event's amplitude. Therefore, SPMM LHF anomalies may either constructively or destructively interfere with coincident ENSO events, thus modulating the amplitude of ENSO. The ocean also plays a role, as the thermally forced SSTA is then advected westward by the mean zonal velocity, generating a warming or cooling in the ENSO SSTA tendency in addition to the wind-forced component. Results suggest that in addition to wind-driven sources, there exists a thermally driven piece to ENSO amplitude and uncertainty that is generally overlooked. Links between the SPMM and Pacific decadal variability are discussed.

1. Introduction

Large SST and tropospheric temperature fluctuations associated with El Niño–Southern Oscillation (ENSO) events can provide enhanced predictability of seasonal climate extremes across the globe (Mo and Schemm 2008; Peng et al. 2012). For instance, ENSO teleconnections influence seasonal forecasts of precipitation and temperature in North America (Infanti and Kirtman 2016; Chen et al. 2017), measures that are valuable for decision support. As such, quantifying the uncertainty of ENSO forecasts is important, as the enhanced predictability of remote climate impacts depends on the strength of the teleconnected ENSO signal. Identifying sources of ENSO amplitude uncertainty and quantifying each source's potential contribution is particularly useful in obtaining a physical understanding of ENSO prediction errors.

The spread of ensemble ENSO predictions is often used to characterize the forecast uncertainty distribution (e.g., Kirtman et al. 2014). Primary sources of uncertainty in ENSO predictions include observational errors in the initial conditions (McPhaden 2003) and noise-driven errors (Xue et al. 1997; Samelson and Tziperman 2001; Karspeck et al. 2006; Larson and Kirtman 2015a,b). Systematic model biases and errors in the representation of the physics (Guilyardi et al. 2009; Bellenger et al. 2014) also contribute to the uncertainty

Corresponding author: Sarah M. Larson, slarson28@wisc.edu

DOI: 10.1175/JCLI-D-17-0722.1

and form the basis of multimodel seasonal climate prediction systems that account for errors in model formulation (Doblas-Reyes et al. 2000; Palmer et al. 2004; Kirtman et al. 2014; Becker and van den Dool 2016).

In general, noise-driven uncertainty in ENSO predictions is forced by anomalous zonal winds (e.g., Karspeck et al. 2006; Lopez and Kirtman 2013; Lopez et al. 2013; Menkes et al. 2014; Levine and McPhaden 2016; Puy et al. 2016; Hu and Fedorov 2018; Larson and Kirtman 2017). The zonal winds can be stochastic or deterministic but the expected ocean response is similar, with the wind stress (hereafter τ) acting as a ''trigger pattern'' that excites equatorial wave dynamics that either constructively or destructively interfere with the ENSO signal (Larson and Kirtman 2017). Such atmospheric wind triggers have a variety of sources including stochastic winds (e.g., weather decoupled from the SSTA; Kleeman and Moore 1997, 1999; Moore and Kleeman 1999), reinforcing winds coupled to the SSTA (e.g., SST state dependent; Eisenman et al. 2005; Gebbie et al. 2007; Tziperman and Yu 2007), and phenomenological variability (i.e., winds originating from a well-known, large-scale phenomenon). Westerly wind bursts (WWBs; e.g., Luther et al. 1983; McPhaden et al. 1992; Harrison and Vecchi 1997), for example, have both stochastic and state-dependent components (Lopez and Kirtman 2013; Lopez et al. 2013). During neutral ENSO conditions, the SSTA has little hold on the overlying atmospheric wind anomalies; therefore, anomalous winds, including WWBs, tend to be stochastic. On the other hand, state-dependent WWBs are common when the west Pacific warm pool extends eastward, providing favorable conditions for successive WWBs (Fedorov 2002; Menkes et al. 2014). A sufficiently strong or persistent WWB can perturb the upper ocean down to the equatorial thermocline, exciting an equatorial Kelvin wave that propagates eastward and influences the eastern Pacific SST (Giese and Harrison 1991; Picaut and Delcroix 1995; McPhaden and Yu 1999; Lengaigne et al. 2002). Noise-driven uncertainty is also generated by the ocean. For example, high-frequency mesoscale ocean variability like tropical instability waves (TIWs) may impact the peak amplitude of an event, as TIWs drive vertical mixing and meridional heat transport (Kessler et al. 1998; Moum et al. 2009; Perez et al. 2012) that influence the cold tongue temperature.

Wind triggers can also be more phenomenological in origin. Studies argue that the North Pacific meridional mode (NPMM; Chiang and Vimont 2004) is a trigger for ENSO events (Chang et al. 2007; Larson and Kirtman 2013) as the atmospheric wind response to the NPMM SSTA is conducive for the excitation of ENSO (Vimont et al. 2003b; Chang et al. 2007; Alexander et al. 2010; Thomas and Vimont 2016). The NPMM is a coupled atmosphere–ocean mode of variability originating in the northeast Pacific, characterized by an anomalous meridional SST gradient and a latitudinal shift of the intertropical convergence zone (ITCZ). The NPMM SSTA, latent heat flux (LHF), and τ signal propagate from the northeast to the central equatorial Pacific via the wind–evaporation–SST (WES) feedback (Liu and Xie 1994; Vimont 2010; Wang 2010b). The generation of the NPMM SSTA signal is thought to be initiated through the seasonal footprinting mechanism (SFM; Vimont et al. 2003a,b; Alexander et al. 2010; Pegion and Alexander 2013), a process by which wind variability driven by boreal wintertime fluctuations in the North Pacific Oscillation (NPO) sea level pressure (SLP) impart an LHF response in the subtropics that forces the SSTA. The SSTA signal then propagates equatorward via the WES feedback. An alternative ''trade wind charging'' mechanism has also been established through a series of papers arguing that the anomalous τ curl generated by the North Pacific SLP fluctuations drives meridional ocean transport in the equatorial Pacific, priming the system for an ENSO event (Anderson 2007; Anderson et al. 2013; Anderson and Perez 2015). A number of mechanisms for ''triggering'' ENSO events associated with North Pacific SLP anomalies are reviewed in Pegion and Selman (2017). Through ensemble model experiments, Thomas and Vimont (2016) demonstrate that the triggering of ENSO events by the NPMM is facilitated through the excitation of equatorial Kelvin waves that then generate a distribution of outcomes that favor ENSO events over neutral events, the statistics of which qualitatively reflect those found in the North American Multi-Model Ensemble (NMME; Kirtman et al. 2014) hindcasts of the NPMM and ENSO (Larson and Kirtman 2014) and a coupled model ensemble study based on the March 2014 and 2015 NPMM-like SSTA initial conditions (Larson and Kirtman 2015a).

An analogous τ triggering argument has since been made for the Southern Hemisphere. The thermally coupled South Pacific meridional mode (SPMM; Zhang et al. 2014a) is characterized by fluctuations in the strength of the southeasterly trade winds in the southeast (SE) Pacific that lead to variations in LHF, ultimately leading to SE Pacific SSTA warming or cooling that then propagates northwestward. Similar to the NPMM, the SPMM extends into the equatorial region via the WES feedback, expanding what begins as warming/cooling in the SE Pacific into the equatorial region. More important for the present study is how studies in the literature hypothesize that SPMM impacts ENSO. Similar to the NPMM, the SPMM is described

as a potential ENSO trigger (Zhang et al. 2014a; Ma et al. 2017; Min et al. 2017), an argument requiring an SPMM-induced τ anomaly in the central Pacific that excites the ocean dynamics necessary for ENSO onset. There is also literature describing how changes in the strength of the Southern Hemisphere subtropical high and the southeast trades (DiNezio et al. 2017; Hu and Fedorov 2018; You and Furtado 2017) can induce SE Pacific SSTA and central equatorial Pacific τ anomalies that are important for Kelvin wave propagation and ENSO amplitude. While these studies generally provide diagnostic analysis as evidence for SPMM and southeast Pacific variability as a potential trigger for ENSO events, the literature remains lacking in rigorous model experimentation, leaving the SPMM–ENSO relationship an open question.

The present study argues for an alternative role for the SPMM in ENSO dynamics, not as a trigger but as a thermally driven source of eastern Pacific SSTA that can occur coincidentally with ENSO events. Results show that in addition to observational errors, model errors, and wind-driven errors, there exists a thermally driven piece to ENSO uncertainty that is generally overlooked. The paper is organized as follows. Section 2 provides the methodology. Section 3 describes the new SPMM–ENSO mechanism. Section 4 provides a summary and discussion.

2. Methodology

The goal of this study is to identify intrinsic sources of ENSO amplitude uncertainty other than the wind-forced dynamical ocean response. The present study focuses on possible thermally driven sources, as they are less explored in the literature. The obvious reason for the lack of literature on this topic is the challenge associated with isolating the thermally driven response while also retaining ocean dynamics and momentum fluxes necessary to simulate realistic ENSO events. To separate the wind-forced response from the thermally driven response, climate model experiments are necessary as such a separation is difficult to do cleanly with observational or model output analysis. We utilize a model configuration specifically designed for such a task (Larson and Kirtman 2015b).

All experiments in this study and a fully coupled control simulation are performed using the National Center for Atmospheric Research (NCAR) Community Climate System Model version 4 (CCSM4; Gent et al. 2011) with a nominal 1° horizontal resolution and pre-industrial forcing. Specifically, we utilize a 100-yr CCSM4 simulation named EnsoWinds (Larson and Kirtman 2018) in which the ENSO variability is perfectly periodic and each ENSO event is forced by identical τ. This way, differences in ENSO events can only arise via two processes: 1) anomalous ocean dynamics unrelated to the prescribed τ and 2) the coupled buoyancy (thermal + freshwater) fluxes. To clarify, the buoyancy fluxes are computed with the atmosphere model-derived winds, not the prescribed τ (discussed below); therefore, they are interactive and coupled with the ocean state. EnsoWinds was used in Larson and Kirtman (2018) to provide initial conditions with various states of subsurface heat content buildup to investigate whether the equatorial recharge/discharge (Jin 1997) contributes to ENSO predictability. EnsoWinds is branched from a CCSM4 control simulation with an already spun up tropical Pacific Ocean.

To generate a repeating ENSO cycle in the model, we use a mechanically decoupled configuration of CCSM4 (Larson and Kirtman 2015b; Larson et al. 2018) in which we prescribe the τ that force the ocean, in this case τ with a repeating ENSO cycle, while leaving all other aspects of the coupled model unconstrained (i.e., the buoyancy fluxes are fully coupled with the ocean state). More specifically, every model day, the ocean experiences daily τ climatology calculated from the free-running control version of CCSM4 with the daily anomalies from a 4-yr ENSO cycle added to the climatology and then repeated. The 4-yr ENSO cycle is obtained from the free-running control (Fig. 1a) and is representative of typical ENSO behavior in the model (Larson and Kirtman 2018).

A stationary ENSO τ anomaly forcing pattern is obtained by the linear regression of the τ anomalies onto the Niño-3.4 (averaged over 5°S–5°N, 170°–120°W) SSTA index over the full control simulation. The amplitude and sign of the forcing pattern are obtained by multiplying the regression pattern $\alpha(x, y)$ by the Niño-3.4 SSTA over the 4-yr ENSO cycle highlighted in Fig. 1a, and then repeated every four years. Figure 1b shows the global τ regression pattern overlaid on SSTA regressed onto Niño-3.4 SSTA. By prescribing the τ forcing on the ocean, the model is no longer mechanically coupled but buoyancy coupling remains active. Most important for this study is that the thermal coupling remains unconstrained, as the atmospheric model–derived winds, not the prescribed winds, are used to calculate the thermal fluxes.

We have demonstrated with previous work that CCSM4 is well suited to study ENSO predictability from various angles, including coupled instability error growth (Larson and Kirtman 2015b), error growth dynamics (Larson and Kirtman 2017), and the role of preconditioning in increasing the signal-to-noise ratio of ENSO events (Larson and Kirtman 2018). We have also

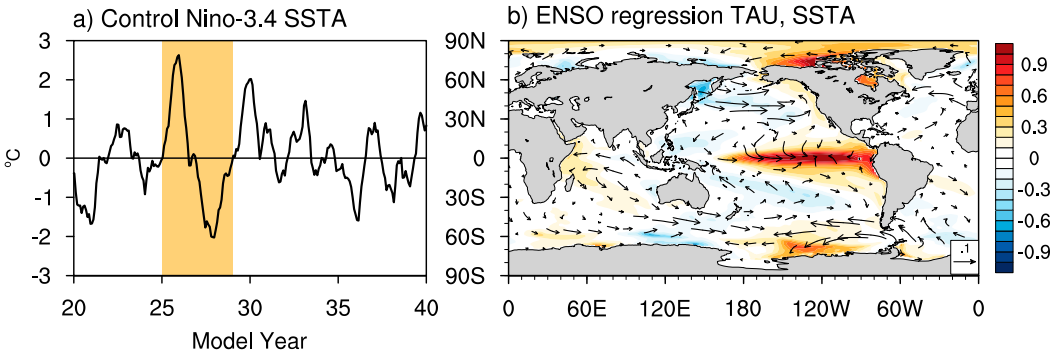

FIG. 1. (a) Control Niño-3.4 SSTA index over 20 arbitrary years. The shaded period highlights the 4-yr ENSO cycle used for the phase-amplitude evolution in EnsoWinds. (b) Vectors show Control ENSO wind stress anomaly pattern calculated as the lag-0 linear regression of wind stress anomalies onto the Niño-3.4 SSTA index. The map is used as the stationary forcing pattern in EnsoWinds. Shading shows similar but with SSTA. Units are dyne cm^{-2} (vectors) and °C (shading) per unit standard deviation of Niño-3.4.

shown that using CCSM4 to model ENSO error growth gives a useful theoretically based benchmark of noise-driven uncertainty that can be supplemented to actual CCSM4 ENSO predictions (e.g., the NMME forecasts; Kirtman et al. 2014). For instance, Larson and Kirtman (2015a) show that the so-called 2014/15 ENSO forecast "bust" was not a bust and was well within the bounds of uncertainty generated via noise-driven processes. Therefore, these studies and the references therein (e.g., Deser et al. 2012; Capotondi 2013; DiNezio and Deser 2014) demonstrate that CCSM4 is an acceptable tool for studying the wind-driven dynamics and growth associated with ENSO. The present study, however, identifies the potential role for a thermally driven source of ENSO uncertainty by removing the possibility that the variations between the simulated ENSO events are due to anomalous τ-driven upper ocean changes. Results are not intended to contradict the rich literature of wind-forced sources of ENSO amplitude uncertainty mentioned in the introduction, as we agree that they are the primary source, but are meant as a secondary source of uncertainty intrinsic to the climate system that may supplement the wind-driven component. We suggest the likely scenario that both wind-driven sources of uncertainty and a thermally driven source may act coincidentally.

For the remainder of the study, fields are averaged over the Niño-3 (5°S–5°N, 150°–90°W) region to isolate differences in the eastern Pacific because equatorial SSTA forced by the SPMM, a phenomenon important in later sections, are concentrated just off the South American west coast. The EnsoWinds Niño-3 SSTA time series shows the perfectly periodic 4-yr ENSO cycle (Fig. 2b). Between each El Niño and La Niña is a neutral-ENSO year, with slight warming or cooling depending on the upcoming phase. Figure 2e shows the canonical ENSO pattern, calculated as the SSTA regressed onto the Niño-3 time series. For reference, Figs. 2a and 2d show similar calculations but for 120 years of the free-running CCSM4 control. The ENSO variability is noticeably less regular than in EnsoWinds. Notice that the peak El Niño event amplitudes in EnsoWinds are similar but not identical and the range of amplitudes differs by approximately 0.5°C. Similar behavior is seen among La Niña events, although El Niño is the primary focus in this study. Understandably, at first glance, the range appears unimpressively small but as a reminder, the differences are not mechanically τ driven, which generates a larger distribution of outcomes in CCSM4 (Larson and Kirtman 2015a,b). How is it possible for ENSO events forced by the exact same τ to have amplitude differences of 0.5°C? We demonstrate that there is an additional source of forcing that supplements the τ-driven ocean response and is worth characterizing.

3. Results

Figure 2c shows the EnsoWinds Niño-3 SSTA *residual* time series, calculated by removing the mean 4-yr ENSO cycle from the SSTA. More specifically, we take the average of all ENSO cycles (defined as evolving in the order El Niño, neutral, La Niña, neutral) in EnsoWinds, and remove that ensemble average from every ENSO cycle. This yields deviations from the ensemble mean ENSO cycle that we refer to as the residual. The residual SSTA, therefore, consists of all variability other than the mean τ-forced ENSO response. The residual Niño-3 SSTA is low amplitude with a 0.12°C standard deviation. The residual time series is independent of the forced ENSO signal, as the correlation between Niño-3 in Figs. 2b and 2c is 0.09. To identify potential coherent structures in the residual, the full SSTAs are regressed onto the residual Niño-3 index (Fig. 2f). The

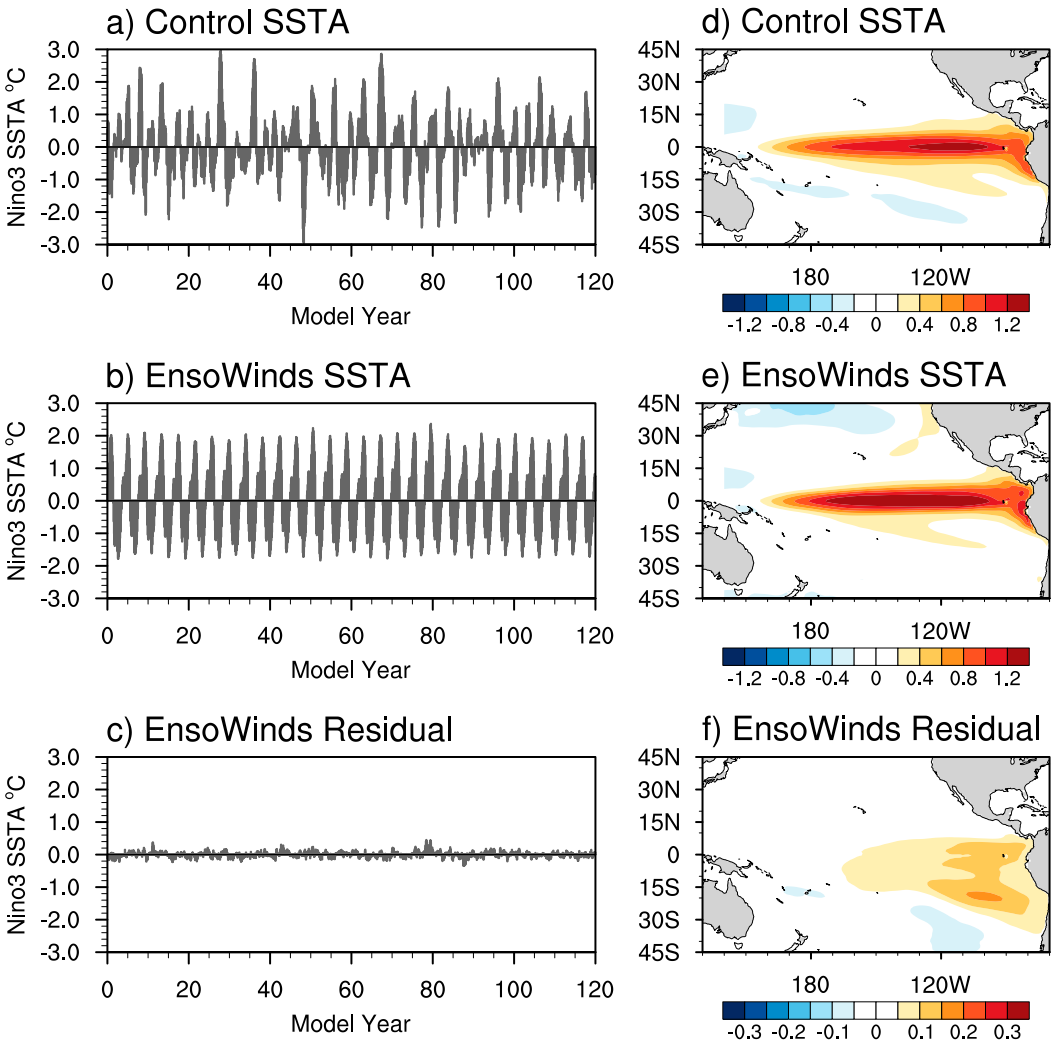

FIG. 2. (a) Control Niño-3 SSTA index and (d) the related SSTA regression pattern, (b) EnsoWinds Niño-3 SSTA index and (e) the related SSTA regression pattern, and (c) EnsoWinds residual Niño-3 SSTA index and (f) the related residual SSTA regression pattern. The residual is calculated by subtracting the mean 4-yr ENSO cycle from the full SSTA. Units in (d)–(f) are °C per unit standard deviation of Niño-3.

pattern consists of maximum eastern Pacific warming between 15° and 30°S that expands northward into the equatorial region.

The resulting pattern is seen in the literature with different names, including the SE Pacific portion of the subtropical dipole (Wang 2010a) and quadrupole modes (Ding et al. 2015), the thermally coupled Walker mode (Clement et al. 2011), and as a snapshot of the South Pacific meridional mode (Zhang et al. 2014a). The pattern is also prevalent in tropical Pacific decadal variability studies (Trenberth and Hurrell 1994; Zhang et al. 1997; Garreaud and Battisti 1999; Yeh and Kirtman 2004, 2006; Vimont 2005; Clement et al. 2011; Okumura 2013; Chen and Wallace 2015; Di Lorenzo et al. 2015). Reconciling the discrepancies in the literature is not the goal of this study, but a hypothesis connecting these two views is provided in the discussion. Taking the existing literature into account, we describe the residual pattern as the SPMM, as we will show that the timing and mechanism are consistent with the SPMM paradigm. Note that the SPMM forcing mechanism is similar to that of the quadrupole mode, as both are described as thermodynamically coupled modes initiated by mid-latitude variability in the South Pacific, essentially the Southern Hemisphere counterpart of the NPMM.

To define a SPMM time series, we compute the pattern correlation of the SPMM pattern in Fig. 2f with the EnsoWinds residual SSTA, which yields a measure of how SPMM-like the residual SSTA appears each month. The full EnsoWinds SSTA is not used, as ENSO

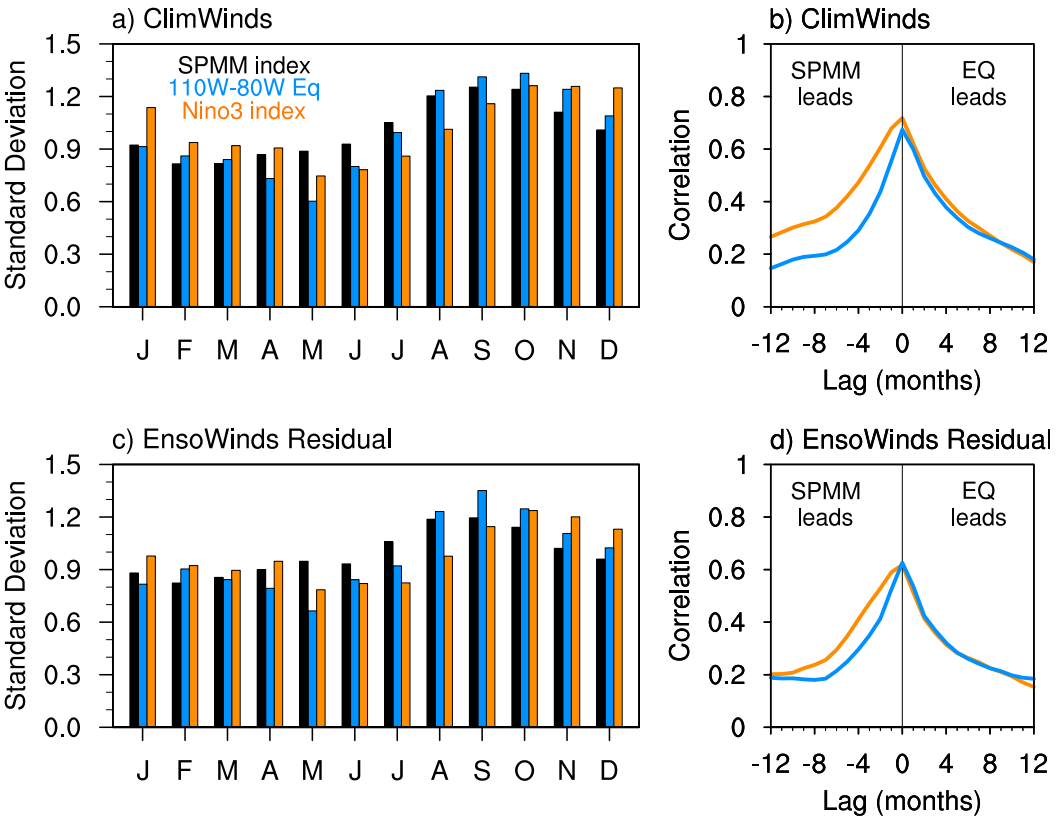

FIG. 3. SPMM seasonality (black) and relationship with equatorial SSTA defined by the Niño-3 SSTA index (orange) and extreme eastern Pacific SSTA (blue). (a) Standard deviation by month of the standardized ClimWinds SPMM index, the Niño-3 SSTA index, and extreme eastern Pacific SSTA averaged over 5°S–5°N, 100°–80°W. (c) As in (a), but for the EnsoWinds residual SSTA. (b),(d) Lead–lag correlation of the SPMM and Niño-3 indexes (orange) and SPMM and 100°–80°W equatorial SSTA (blue) in (a) and (c), respectively. Positive lags indicate the equatorial (EQ) SSTA index leads.

amplitude dominates over the lower-amplitude SPMM. For comparison, Fig. 3c shows the standard deviation of both the SPMM index and the residual Niño-3 SSTA for each calendar month. Both time series are first scaled by their respective standard deviation. The peak variability in the SPMM occurs in September, whereas the peak residual Niño-3 variability occurs in October. The maximum lead–lag correlation between the SPMM and Niño-3 indexes occurs at lag 0 (Fig. 3d). Why does the peak Niño-3 variability lag the peak SPMM variability by 1–2 months if their maximum correlation is at lag 0? When the SPMM SSTA is strongest, its *thermally forced* Niño-3 SSTA footprint is largest. We will show in section 3b that the mean zonal current also has an impact on the Niño-3 SSTA tendency. The variability in the Niño-3 domain is largest once westward advection by the mean zonal current spreads the (SPMM induced) thermally forced SSTA through the full domain. The time it takes for the SSTA signal to spread through the full Niño-3 domain is 1–2 months. Therefore, although temporally the SPMM and Niño-3 have a maximum covariability at lag 0 when the SPMM thermal forcing of the Niño-3 SSTA is at a maximum, the amplitude of the variability throughout the full Niño-3 is larger, on average, once the signal spreads westward via the ocean circulation. If instead we average over the extreme eastern domain 5°S–5°N, 110°–80°W (blue bars; Figs. 3c) where the initial SPMM thermally forced SSTA occurs, the maximum variability occurs in September, similar to the SPMM.

What is most important is characterizing the mechanism (i.e., the SPMM) that generates the spread of El Niño events in EnsoWinds and then detailing how the SPMM impacts the actual amplitude of events. Recall that subtropical meridional modes are described as ENSO ''triggers'' (Chang et al. 2007; Larson and Kirtman 2013; Zhang et al. 2014a; Min et al. 2017; Thomas and Vimont 2016), which implies that a τ-induced dynamical ocean response is invoked in the mechanism. However, this mechanism is eliminated in the EnsoWinds experiment and cannot contribute to the

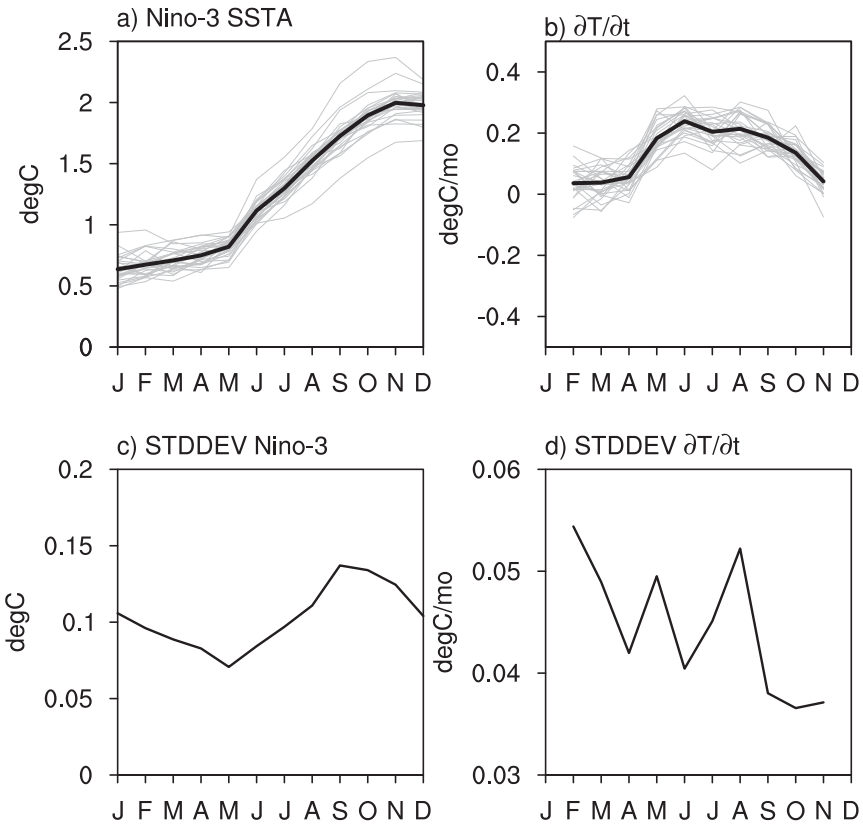

FIG. 4. (a) Niño-3 SSTA evolution of the 30 El Niño events in EnsoWinds, (b) the SSTA tendency, (c) the standard deviation of the Niño-3 SSTA, and (d) the standard deviation of the SSTA tendency.

spread of El Niño events. Therefore, the results here are a new contribution to how the SPMM may influence ENSO.

The timing of when the El Niño events diverge will give clues as to whether the SPMM is indeed the forcing mechanism. To see when the El Niño events diverge, the Niño-3 SSTA evolution of each El Niño event (30 in total) is shown in Fig. 4a. The Niño-3 standard deviation over the events (i.e., the spread) is largest in September (Fig. 4c) when the standard deviation of the SPMM index is at a maximum (Fig. 3c), although the maximum standard deviation in the SST tendency occurs in August (Fig. 4d). As an example, Figs. 5a and 5c show the September SSTA of the strongest and weakest El Niño event. El Niño event strength is ranked by the September (when the spread is largest) Niño-3 SSTA; however, the same strongest and weakest events would be selected whether any month from September to December was chosen. Large sample composites will be shown using a different dataset in section 3a. Given that the sample size in EnsoWinds is small, the extremes are shown here to exemplify the potential effects of the SPMM on individual event amplitude and spatial structure.

Note that the τ anomalies shown in Fig. 5 are obtained from the atmospheric model output. To be clear, this is the τ the ocean would experience had we not overwritten it with prescribed values as per the methodology in section 2. The atmosphere-model-derived winds, not the prescribed climatology, are also used in the model formulation of the heat fluxes. The warm SSTA for the strongest El Niño extends southward through the subtropics, whereas the weakest event is meridionally confined to the equatorial band with cooler SSTA in the SE Pacific. The residual (mean ENSO cycle removed) SSTA is shown in Figs. 5b and 5d. The residual September SSTA for the strongest El Niño shows the positive phase of the SPMM, whereas that for the weakest El Niño shows the negative phase of the SPMM. It is obvious that the residual patterns in the southeast Pacific are consistent with the SPMM pattern and the timing is similar to when SPMM is most variable (Fig. 3c).

a. SPMM latent heat flux forcing

If the SPMM is characterized by SE Pacific warming, how does it impact the amplitude of ENSO events? To better understand how the SPMM may interact with the

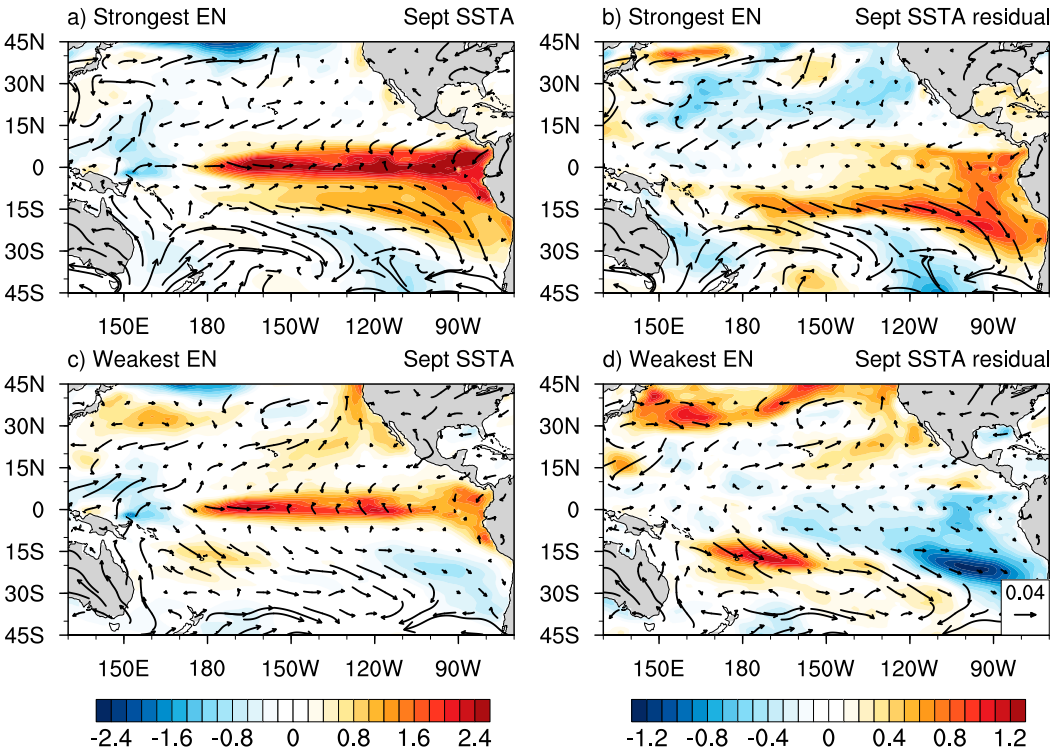

FIG. 5. September SSTA in °C and wind stress anomalies in N m^{-2} from the (a) strongest and (c) weakest El Niño event in EnsoWinds. Events are ranked by the September Niño-3 SSTA index, as September exhibits the largest standard deviation of Niño-3. (b),(d) As in (a),(c), but for the EnsoWinds residual SSTA calculated by subtracting the mean 4-yr ENSO cycle from the full SSTA. Wind stress anomalies are obtained from the atmospheric model output and are representative of the winds used in the model formulation of the heat fluxes. This is not the anomalous wind stress the ocean experiences, as it is prescribed per the methodology described in the text, but rather the uncoupled atmospheric response to the SSTA.

τ-forced ENSO response, a longer SPMM time series is needed for more robust conclusions. We next utilize 500 years of a CCSM4 simulation named ClimWinds [Larson and Kirtman 2015b, 2018; also see DailyWinds and MonthlyWinds in Larson et al. (2017)] in which the global ocean only experiences τ climatology. The simulation is identical to EnsoWinds with the exception that there are no anomalous ENSO-related τ forcing the ocean. As a result, ClimWinds is perpetually ENSO neutral. ClimWinds is a helpful simulation for piecing apart the SPMM mechanism and how it may influence ENSO for two reasons. First, prior modeling studies leave the question open as to whether ocean dynamics are important in the oceanic response to the thermally coupled SPMM (Zhang et al. 2014a). ClimWinds includes the possibility for anomalous ocean heat transport. Second, how the SPMM operates in a coupled model in the absence of ENSO signal interference is of particular interest because the two modes overlap spatially. ClimWinds does not support canonical ENSO variability but does support the SPMM mechanism.

ClimWinds differs from a traditional slab ocean mixed-layer (SOM) version of CCSM4 in a few key ways. The obvious difference is that the ocean component of the SOM is a mixed-layer slab ocean model (see Bitz et al. 2012) in which the SST tendency is driven by the net heat fluxes and a prescribed ocean heat transport convergence computed from the fully coupled CCSM4. ClimWinds instead includes a dynamical ocean model. Since the ocean component of ClimWinds is forced by climatological τ, ClimWinds simulates the mean ocean circulation as well as anomalous ocean heat transport convergence unrelated to the prescribed τ. Unlike the prescribed mixed layer depth (MLD) in the SOM, the MLD in ClimWinds freely evolves. Both the SOM and ClimWinds are thermodynamically coupled and neglect anomalous wind-driven Ekman advection. In the SOM, SST variability in the ENSO region is driven by heat fluxes. What is different about ClimWinds is that once the SST anomalies are forced by heat fluxes, the ocean circulation can advect those anomalies around. ClimWinds also simulates TIWs, which increase SST mixing in the eastern equatorial Pacific. Averaged over the

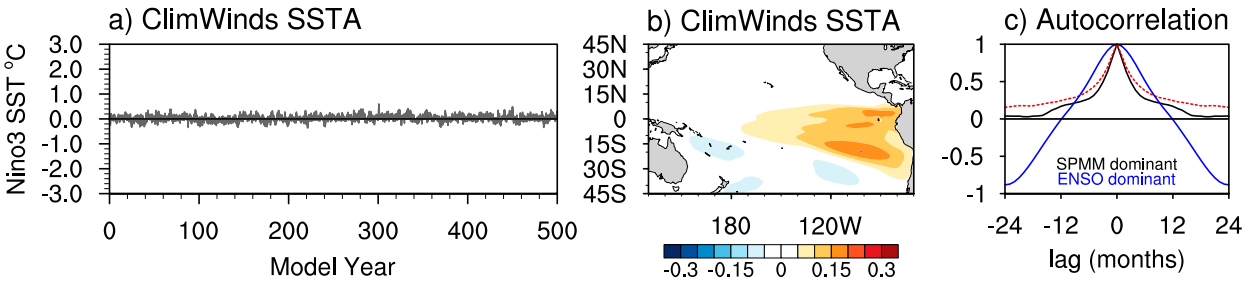

FIG. 6. (a) ClimWinds Niño-3 SSTA index and (b) the SSTA regression pattern. Units in (b) are °C per unit standard deviation of Niño-3. (c) Autocorrelation of the Niño-3 SSTA in EnsoWinds (blue), EnsoWinds residual (black), and ClimWinds (red dashed). In EnsoWinds, the dominant forcing of Niño-3 SSTA is ENSO. In the EnsoWinds residual SSTA, defined as removing the mean 4-yr ENSO cycle from the full SST, the dominant forcing of the Niño-3 SSTA is the SPMM. In ClimWinds, the dominant forcing of the Niño-3 SSTA is the SPMM.

Niño-3 domain, the ClimWinds SSTA tendency has a 0.6 correlation with anomalous net surface heat fluxes and a 0.5 correlation with anomalous LHF. This means that the primary driver of the Niño-3 SSTA is latent heating with a secondary role for ocean dynamics, both of which are important mechanisms in describing the differences in amplitudes of the El Niño events in EnsoWinds.

Figure 6 shows the Niño-3 SSTA time series and regression patterns for ClimWinds. ClimWinds produces a Niño-3 SSTA time series with a nearly identical standard deviation (0.11°C) as the EnsoWinds residual Niño-3, as well as similar spatial structure (cf. Figs. 6a,b and 2c,f). In other words, the residual SSTA in EnsoWinds and the SSTA in ClimWinds are both forced by the SPMM. Note that the ~0.1°C Niño-3 standard deviation in ClimWinds is roughly half that seen in the SOM version of CCSM4 (L. Murphy 2016, personal communication). The reduced amplitude can be attributed to advection of the thermally driven SSTA by the mean ocean circulation and increased mixing due to TIWs, both mechanisms that are lacking in SOMs. The autocorrelations of the ClimWinds and EnsoWinds residual Niño-3 SSTAs (Fig. 6c; both SPMM dominant) are distinctly different from the EnsoWinds full SSTA (ENSO dominant), further demonstrating the similarity between ClimWinds and the EnsoWinds residual. Similar to the residual SPMM index, an SPMM index for ClimWinds is calculated by the pattern correlation of the SPMM pattern (Fig. 6b) and the monthly ClimWinds SSTA. Consistent with the residual SPMM index, the peak variability in the ClimWinds SPMM index occurs in September (Fig. 3a) and the maximum lead–lag correlation between the SPMM and Niño-3 occurs at lag 0. Based on these similarities, the ClimWinds SSTA will be used to produce more robust composites of the SPMM-forced evolution of the eastern equatorial Pacific because of both the abundance of simulation years (500+ years) and the lack of ENSO signal interference that may mask the SPMM anomalies in EnsoWinds.

Based on an empirical orthogonal function (EOF) analysis of the ClimWinds SSTA in the domain 30°S–30°N, 140°E–70°W (not shown), the SPMM mode, consisting of the sum of EOF 2 and 3, is the only mode of variability among the first six EOFs that projects onto equatorial Pacific SSTA. Modes 2 and 3 combine to produce just under 20% of the variance in ClimWinds in this domain. The first EOF, explaining 11% of the variance, is the NPMM and EOFs 4–6 are characterized by subtropical SSTA without an equatorial footprint. Although the SPMM is not the dominant variability between 30°S and 30°N in the Pacific, it is the only variability that projects onto the equatorial Pacific and as a result, is the dominant driver of SST variability in the ENSO region. Regressing SSTA onto the principal component time series for EOF1 of SSTA in the Niño-3 domain confirms that the dominant variability in the eastern equatorial Pacific in ClimWinds is associated with the SPMM.

Composite evolutions of LHF, SST, and τ anomalies for the SPMM are shown in Fig. 7. The τ anomalies are obtained from the atmospheric model output, as the atmospheric model-derived winds are used in the model LHF calculation. Recall that in ClimWinds, the momentum fluxes into the ocean are calculated with the prescribed climatological τ (no anomalies). Therefore, the τ composites shown can only be used to explain the LHF anomalies and the atmospheric response to the SSTA. Composites are calculated by subtracting the average of the 50 coldest SPMM cases from the average of the 50 warmest SPMM cases and then dividing by 2. SPMM events are ranked by the September SPMM index, the timing of peak SPMM variability. Results are consistent when ranking the events using any month from September to December. Results are also consistent when using the Niño-3 index instead of the SPMM

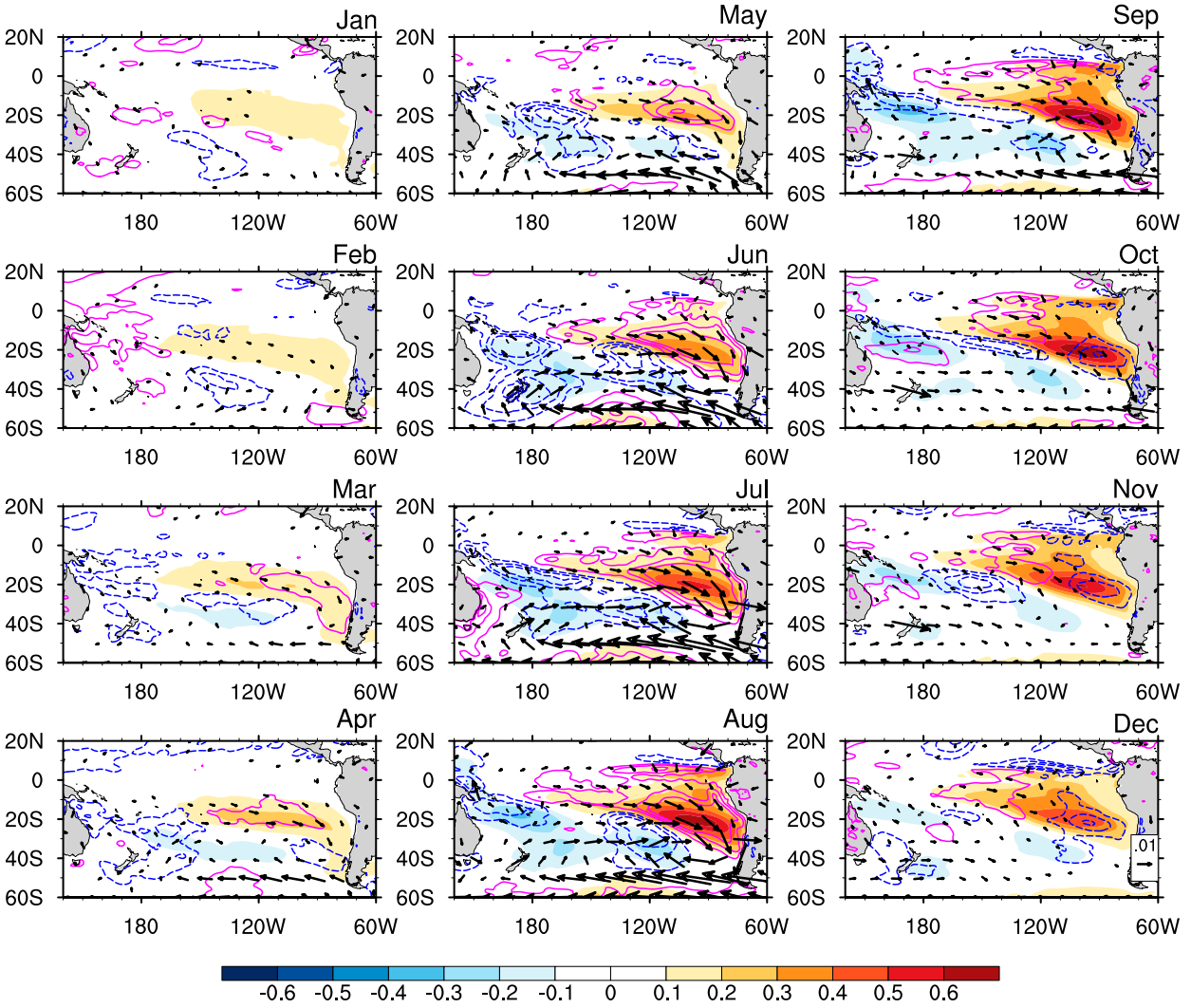

FIG. 7. SPMM composites of SSTA, LHF anomalies, and surface wind stress in ClimWinds. ClimWinds has no ENSO variability. Composite averages are calculated by subtracting the average of the 50 coldest events from the average of the 50 warmest events then dividing by 2. SPMM events are ranked by the September SPMM index. SSTA is in °C (shading) and wind stress is in N m^{-2} (vectors). LHF anomaly contours are −9, −6, and −3 (blue dashed) and 3, 6, and 9 (pink) W m^{-2}. Only wind stress anomalies of magnitude 0.002 N m^{-2} or larger are shown.

index, rather unsurprising given that the maximum correlation (~0.7) between the SPMM and Niño-3 occurs at lag 0 in ClimWinds.

The January–February composites show weak warm SSTA and weak westerlies south of the central equatorial Pacific due to periods of more persistent SPMM patterns. Boreal springtime is instead considered the onset of the SPMM, as the dynamics and the initial forcing (see section 4) become clear during this time. During March–May, westerlies south of the central equatorial Pacific and northwesterlies in the SE Pacific appear and strengthen. The τ anomalies oppose the mean wind direction, thus reducing the total wind speed and according to the SPMM mechanism, resulting in reduced evaporation and positive (downward) LHF anomalies. The positive LHF response is evident in the May composite. At the same time, anomalous easterlies strengthen near 50°S and τ anomalies form an anomalous cyclone by June. The pattern indicates weakening of the subtropical high as described by Wang (2010a) with the dipole mode and by Okumura (2013) with Pacific decadal variability. As the subtropical high weakens, the anomalous northwesterlies strengthen, further contributing to the intensification of the LHF warming in the SE Pacific. In June, northerly τ along the equator flowing toward the warm SSTA in the SE Pacific first appear, indicating that the WES feedback is expanding the SPMM equatorward

(Zhang et al. 2014a). By July, positive LHF and weak SSTA warming appear in the eastern equatorial Pacific where the northerly equatorial τ appeared in June. In addition, northerly τ anomalies form north of the equator for the first time. In August, positive LHF drives further SSTA warming. The northward expansion of τ and positive LHF associated with the WES feedback continues to strengthen the SPMM signal forming in the eastern equatorial Pacific. The positive LHF anomalies peak in the Niño-3 region in August–September and the peak SSTA follow one month later. This point will be shown more definitively below. Negative LHF anomalies form shortly after and act as a damping to the SPMM pattern. The timing in Fig. 7 is consistent with the evolution of the SPMM in slab ocean models as described in Zhang et al. (2014a), with first a weakening of the surface winds that induce LHF warming and then propagation of the signal across the equatorial eastern Pacific into the NH via the WES feedback.

Since we are primarily interested in the SPMM-forced eastern equatorial Pacific, Fig. 8 shows the lagged regression of the EnsoWinds residual (mean ENSO cycle removed) Niño-3 SSTA with Niño-3 LHF anomalies the months prior (i.e., "SPMM dominant" black curve). Positive SSTAs are most closely linked to positive LHF anomalies one month prior. The LHF eventually becomes a weak damping (negative) when the LHF lags the SSTAs (not shown). The red dashed curve shows the same calculation with ClimWinds SSTAs and LHF anomalies. The close similarity between the ClimWinds and EnsoWinds residual calculations verify that both datasets represent the SPMM. The relationship between LHF and SSTA in Fig. 8 adds further evidence that the LHF forces the ocean, consistent with the SPMM mechanism. This is distinctly different from the relationship between LHF and SSTA seen in EnsoWinds ("ENSO dominant" curve) when using the full anomaly, as the LHF clearly acts as a damping term due to the dominant ENSO signal. Since SPMM is definitively independent of ENSO as evidenced by its presence in ClimWinds, then the two mechanisms, SPMM and ENSO, with very different roles for LHF, may operate coincidentally as seen in EnsoWinds. Although the amplitude of LHF anomalies associated with ENSO are an order of magnitude larger than those of SPMM, depending on the sign of the SPMM, the associated LHF anomalies may either constructively or destructively interfere with the (damping) ENSO LHF, impacting the SSTA tendency.

Note that Zhang et al. (2014a) argue that shortwave cloud forcing (SWCF) plays a role in the SPMM evolution and heat flux forcing of the SSTA. When the

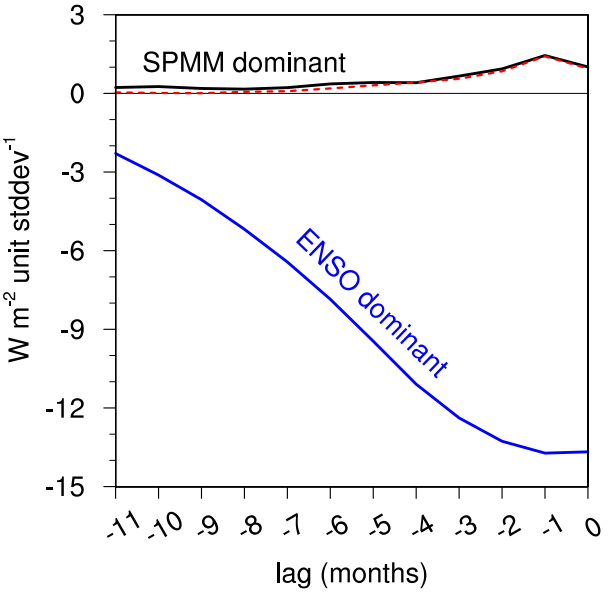

FIG. 8. Lagged regression of Niño-3 LHF anomalies and standardized Niño-3 SSTA in W m^{-2} per unit standard deviation of Niño-3 SSTA. Negative lag indicates LHF leads the SSTA. The blue curve is computed using SSTA and LHF anomalies from EnsoWinds, in which the dominant mechanism in the Niño-3 region is ENSO. The black curve is computed using the EnsoWinds residual SSTA and LHF anomaly fields, in which the dominant mechanism in the Niño-3 region is forced by the SPMM. The residual SSTA is calculated by removing the mean 4-yr ENSO cycle from the full SST. The red dashed curve is computed using SSTA and LHF anomalies from ClimWinds (no ENSO variability), in which the dominant mechanism in the Niño-3 region is forced by the SPMM.

SWCF anomalies are added to the LHF anomalies in Fig. 8, the magnitude of the regression values increases slightly (not shown), verifying that SWCF and LHF anomalies tend to be in phase leading up to peak SPMM (see Zhang et al. 2014a, their Fig. 2b). That said, overall, the change is small, confirming that LHF forcing is the dominant SPMM-induced heat flux forcing of the Niño-3 SSTA. For this reason, we only include LHF in the analysis, not to discount the importance of cloud forcing, but to highlight the dominant mechanism.

If the SPMM is indeed the cause of the enhanced El Niño spread, the LHF anomalies associated with the El Niño events should reflect the influence of the SPMM-driven LHF anomalies in the Niño-3 region. Since the SPMM-forced Niño-3 SSTA lags the LHF by one month (Fig. 8), we look to the August LHF anomalies in EnsoWinds, as they lead the maximum El Niño SSTA spread in September. The scatterplot of the residual August LHF anomalies and September SSTA (Fig. 9b) from the El Niño events in Fig. 4a show a positive linear relationship, with relatively warmer (cooler) September

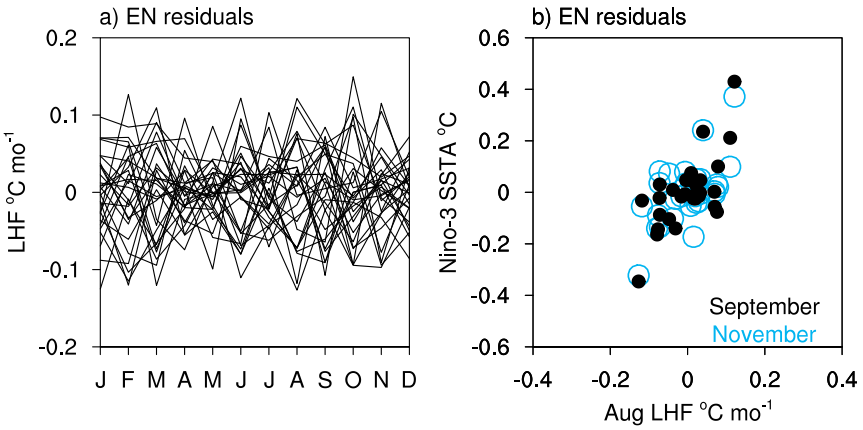

FIG. 9. (a) LHF anomaly evolution of the 30 El Niño events in EnsoWinds. (b) Scatterplot of August LHF anomalies averaged over the Niño-3 region and the September (black dots) and November (blue circles) Niño-3 SSTA of the events in (a). All values are EnsoWinds residuals and show deviations from the mean wind-forced ENSO cycle.

SSTA preceded by anomalous positive (negative) LHF anomalies in August. During an El Niño event, the LHF acts as a damping; therefore, Fig. 9b shows that the stronger El Niño events experience reduced LHF damping compared to the ensemble mean (positive anomaly), whereas the weaker El Niño events experience enhanced LHF damping (negative anomaly). Whether the LHF anomaly destructively or constructively contributes to the LHF damping of the coincident El Niño event is directly tied to the SPMM. Specifically, an El Niño event occurring coincidentally with positive phase SPMM (as in Fig. 5b) can grow more intense as the SPMM-induced positive LHF anomaly opposes a fraction of the SSTA damping. Instead, if the SPMM is in a cool phase (as in Fig. 5d), the SPMM LHF cooling is in phase with the LHF damping associated with the coincident El Niño event, reducing the event's overall amplitude. A similar but weaker positive relationship is seen in the November SSTA (Fig. 9b, blue circles), as the SPMM is undergoing the decay phase.

b. The role of ocean advection

If SPMM-forced LHF anomalies are the only important difference in the El Niño event amplitudes, then the Niño-3 LHF anomaly evolution for the individual events should show a similar increase in the spread as the Niño-3 SSTA (Fig. 4a). Figure 9a shows that instead the atmospheric signal is noisy and more variable, rather unsurprising given that LHF variations due to atmospheric noise are also present. How does the spread in the Niño-3 SSTA signal become so smooth? An obvious pathway is through the ocean. Essentially, the LHF anomalies may provide the initial SSTA forcing, but ocean advection provides the slower, smoother response that is reflected in the Niño-3 time series.

An interesting observation is how the equatorial SSTAs behave once the SPMM warming forms in the extreme east Pacific. The SSTAs appear to expand westward beginning in July (Fig. 7). The following anomalous horizontal advection terms from the surface layer temperature budget are calculated to quantify the effects of surface layer (h) advection on the SSTA tendency:

$$\mathrm{Adv}'_x = -\frac{1}{h}\left(\int_{-h}^{0} u'\frac{\partial \overline{T}}{\partial x}dz + \int_{-h}^{0} \overline{u}\frac{\partial T'}{\partial x}dz + \int_{-h}^{0} u'\frac{\partial T'}{\partial x}dz\right), \tag{1}$$

$$\mathrm{Adv}'_y = -\frac{1}{h}\left(\int_{-h}^{0} v'\frac{\partial \overline{T}}{\partial y}dz + \int_{-h}^{0} \overline{v}\frac{\partial T'}{\partial y}dz + \int_{-h}^{0} v'\frac{\partial T'}{\partial y}dz\right), \tag{2}$$

where Adv'_x and Adv'_y are the anomalous zonal and meridional advection, respectively, u and v are zonal and meridional velocities, respectively, $h = 10$ m, the overbar denotes the seasonal cycle mean, and the prime denotes the anomaly. Similar results are obtained with $h = 20$ m. Vertical advection is not included since vertical velocity is very small near the surface. All terms on the right-hand side of (1) and (2) are computed for each El Niño event and ClimWinds and shown in Fig. 10.

The two terms generating the most variability in ClimWinds, $-\overline{u}\partial T'/\partial x$ and $-\overline{v}\partial T'/\partial y$, are tied to the mean ocean circulation. In spring, the mean horizontal currents are seasonally strong (Larson et al. 2017) in the ENSO region in CCSM4, driving larger horizontal

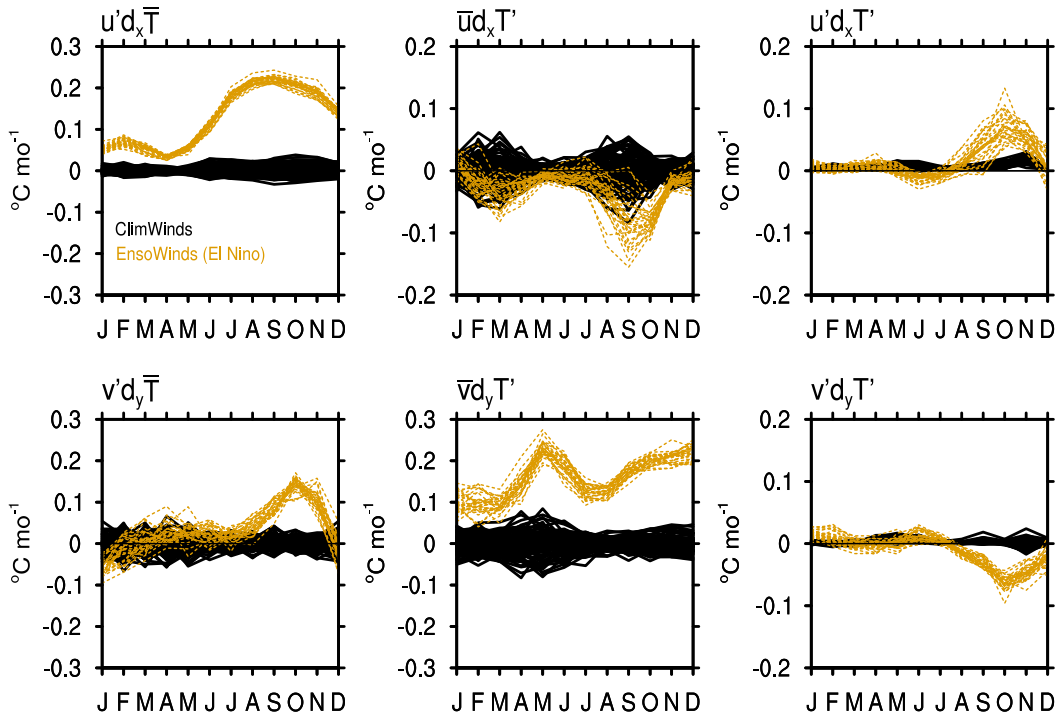

FIG. 10. Niño-3 averaged zonal and meridional advection terms from the surface temperature equation, calculated for the 30 El Niño events in EnsoWinds (gold) and ClimWinds (black). The prime denotes the anomaly and the overbar represents the climatological seasonal cycle.

temperature advection by the mean circulation. In fall, however, the only term generating considerable variability is $-\overline{u}\partial T'/\partial x$. At this time, not only is the mean ocean circulation contributing, as the mean zonal current is at its annual maximum intensity, but SSTA variability in the ENSO region is also seasonally large (Fig. 3a). Since the SPMM is the primary driver of eastern equatorial Pacific SSTA variability during this time, we expect that the SPMM is thermally driving SSTA that is then advected by the mean zonal current. If the SPMM is indeed the mechanism modulating the intensity of the El Niño events in EnsoWinds and generating spread in the Niño-3 SSTA (Fig. 4c), then $-\overline{u}\partial T'/\partial x$ should be the primary term from Eqs. (1) and (2) generating spread among the El Niño events (gold) in Fig. 10. This is the case.

It is intuitive that mean zonal advection of anomalous temperature $-\overline{u}\partial T'/\partial x$ is the ocean mechanism connected to the increased Niño-3 SSTA spread. For example, the $-\overline{u}\partial T'/\partial x$ term is almost always negative during El Niño events. The mean zonal velocity is westward $\overline{u} < 0$ during this time (Larson et al. 2017) and because the maximum warming associated with El Niño is not directly adjacent to the South American coast (Figs. 2d,e), $\partial T'/\partial x$ is negative in much of the Niño-3 domain, thus resulting in $-\overline{u}\partial T'/\partial x < 0$. Additional positive phase SPMM-induced SSTA warming occurs in the extreme eastern Pacific, and so $\partial T'/\partial x$ becomes less negative or near zero as the warm SSTA becomes more zonally ubiquitous (as in Fig. 5a). As such, $-\overline{u}\partial T'/\partial x$ becomes less negative or near zero. If SPMM is instead in a cold phase during El Niño onset, $\partial T'/\partial x$ becomes more negative (as in Fig. 5b), resulting in a more negative $-\overline{u}\partial T'/\partial x$. The spread in this term is small until around August. As seen in Fig. 7, the LHF anomalies associated with the SPMM finally reach the Niño-3 region by July, and drive changes in the SSTA the following month (Fig. 8), in this case August. As the SPMM-induced SSTA warms or cools, the anomalies are contemporaneously advected westward with the mean zonal current which is at maximum strength in August–September in CCSM4 (Larson et al. 2017). As such, the spread in $-\overline{u}\partial T'/\partial x$ remains small through July due to relatively smaller values of $\overline{u}$ and $\partial T'/\partial x$ but begins increasing in August. The spread is largest in September, when both the SPMM variability is largest and the maximum SPMM-forced Niño-3 SSTA occurs. The spread decreases after September, as the strength of the SPMM declines and the mean zonal current seasonally weakens. Similarly, the spread in the Niño-3 SSTA (Fig. 4c) decreases following the September peak. Because ocean surface velocities are largely wind driven,

the other Adv_x terms show little spread since the anomalous wind forcing is identical for each event. The Adv_y terms appear to have little influence as well.

The possibility of a role for mean advection in the SPMM mechanism is mentioned in Zhang et al. (2014a), although as a potential means for northward expansion of the SPMM. The present study shows that mean advection actually transports the SPMM SSTA signal westward (Fig. 10), affecting a larger zonal expanse of the equatorial eastern Pacific. The mean zonal current over the Niño-3 region in CCSM4 is too weak compared to reanalysis products (Larson et al. 2017); therefore, in nature, $-\overline{u}\partial T'/\partial x$ may have a larger contribution to the SSTA tendency, further exaggerating the SPMM's influence on the spread. That said, models that ignore Ekman advection, like SOMs and mechanically decoupled configurations, tend to overestimate subtropical SSTA variance (Larson et al. 2018); therefore, SPMM strength could be slightly weaker in nature compared to EnsoWinds and ClimWinds (both neglect Ekman advection), ultimately affecting the intensity of the Niño-3 SSTA. These two factors likely cancel out to some extent but are worth mentioning. It is also possible that the sign of $-\overline{u}\partial T'/\partial x$ could be positive in a model that simulates the maximum ENSO SSTA variance closer to the South American coast, and $\partial T'/\partial x$ would instead be positive during El Niño. Nevertheless, the spread about the mean ENSO signal due to the SPMM would still reflect the LHF forcing.

4. Summary and discussion

The role of thermally driven ocean processes in modulating the amplitude and spread of El Niño events is a relatively unexplored topic. The present study argues that in addition to wind-driven variability, thermally driven variability also contributes to ENSO amplitude and uncertainty. We utilize a CCSM4 simulation named EnsoWinds (Larson and Kirtman 2018) in which the ENSO variability is perfectly periodic and each El Niño event experiences identical τ forcing. The simulation is mechanically decoupled (Larson and Kirtman 2015b; Larson et al. 2018); therefore, differences in the amplitude of ENSO events can only be explained by buoyancy (thermal + freshwater) fluxes and/or anomalous ocean dynamics decoupled from the prescribed τ. The amplitude differences among El Niño events range 0.5°C, so this thermally driven piece is not trivial.

Analysis reveals that the mechanism contributing to the El Niño spread is the thermodynamically coupled South Pacific meridional mode (SPMM; Zhang et al. 2014a). The SPMM is characterized by fluctuations in the strength of the southeasterly trade winds in the SE Pacific that lead to variations in LHF, ultimately impacting the SSTA. The SPMM grows via the WES feedback, expanding what begins as warming/cooling in the SE Pacific into the equatorial eastern Pacific. The timing of the SPMM in the present study is consistent with the slab ocean mixed-layer models in Zhang et al. (2014a). Instead, when mechanical coupling is allowed as in a fully coupled model or observations, the SPMM peaks in boreal winter (Zhang et al. 2014a; Min et al. 2017). We briefly address the proposed reasons for this discrepancy mentioned in Zhang et al. (2014a). The lack of a seasonally varying MLD is a significant difference between slab ocean and fully coupled models. The MLD in the southeast Pacific is shallower in ClimWinds and EnsoWinds during boreal fall compared to the fully coupled control version of the model, therefore, the MLD could contribute to why ClimWinds and EnsoWinds SPMM peak early. ENSO may also influence the timing of the SPMM (Zhang et al. 2014a). SPMM could be coupled to ENSO through the lower-level circulation (Toniazzo 2010), although the SPMM in EnsoWinds does feel the surface stress associated with the ENSO signal (Fig. 1b) and the timing still differs. This suggests that the atmospheric response to the SSTA and how it feeds back to the ocean may be important when the two modes occur coincidentally and that mechanical coupling could shift the timing of the peak SPMM. Therefore, the SPMM–ENSO mechanism in the present study may play an even larger role in ENSO amplitude and uncertainty if including momentum coupling or a deeper MLD shifts the SPMM peak timing to boreal winter.

How the SPMM directly influences ENSO amplitude is the new contribution of the present study. Previous studies argue that meridional modes, originating from both the North and South Pacific, act as ENSO ''triggers'' (Chang et al. 2007; Larson and Kirtman 2013; Zhang et al. 2014a; Min et al. 2017; Thomas and Vimont 2016), an argument that implies a wind-forced upper ocean response. Here we argue that the LHF anomalies associated with SPMM may constructively or destructively interfere with a coincident ENSO event, affecting the magnitude of the LHF damping of the event, thus directly impacting the overall SSTA amplitude of ENSO events. Analysis shows that when an El Niño event occurs coincidentally with positive phase SPMM, the positive LHF anomaly associated with the SPMM counteracts a fraction of the LHF damping of the event in the Niño-3 region, allowing for a more intense El Niño. On the other hand, if an El Niño event occurs coincidentally with negative phase SPMM, the SPMM-induced negative LHF anomalies enhance the LHF damping of the event, reducing the overall amplitude of

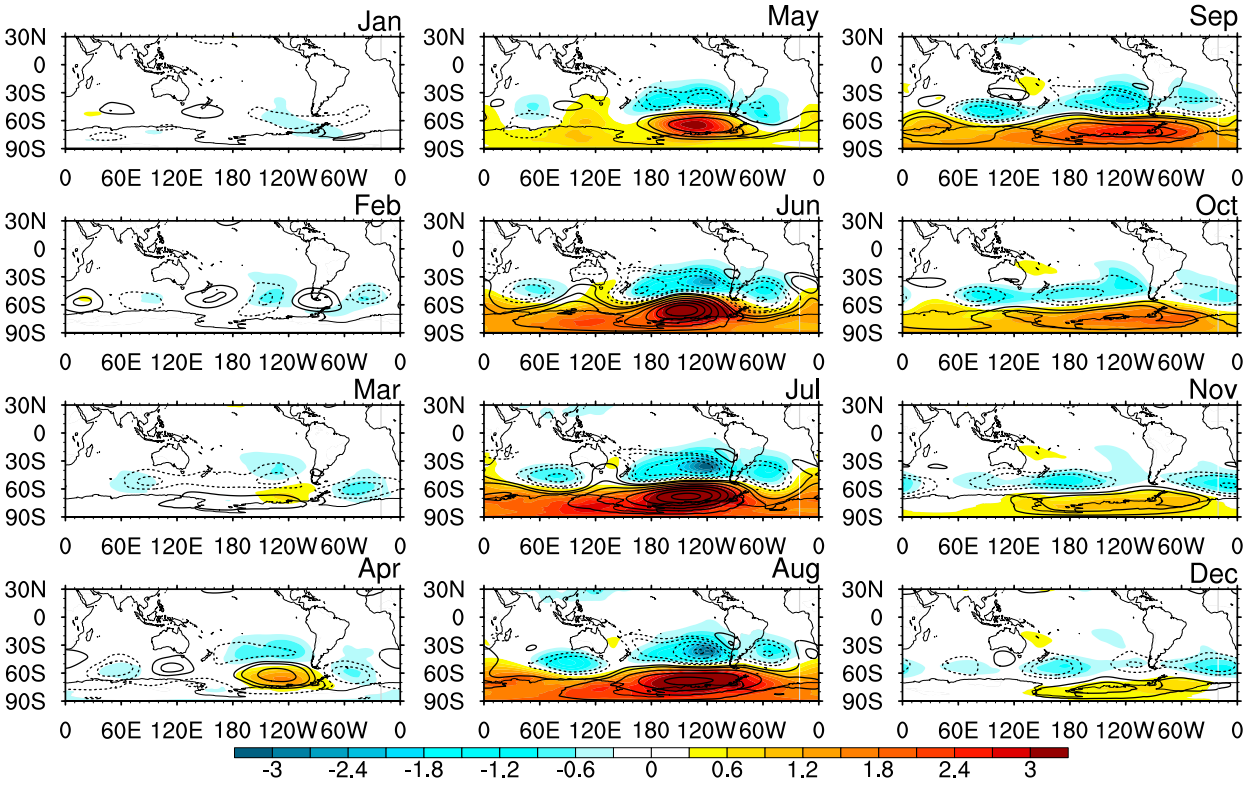

FIG. 11. As in Fig. 7, but with sea level pressure anomalies in hPa (shading) and 500-hPa geopotential height anomalies in meters (contours) with positive and negative contours of 5, 10, 20, and so on in increments of 10 m.

El Niño. An analogous argument for La Niña also holds, with the cool (warm) phase SPMM coincident with La Niña resulting in a relatively larger (smaller) La Niña amplitude.

The evolution of the Niño-3 LHF anomaly for the El Niño events does not, however, explain the smoother evolution of the Niño-3 SSTA spread. Instead, the ocean also plays a role in transporting the SPMM-forced SSTA signal westward, ultimately impacting the SST tendency throughout the Niño-3 region. Mean westward zonal advection of anomalous temperature $-\overline{u}\partial T'/\partial x$ is responsible for spreading the SPMM SSTA signal away from its initial forcing. To summarize, the peak amplitude differences between the (identically τ forced) El Niño events are due to LHF anomalies associated with the SPMM driving SSTA warming/cooling in the extreme eastern Pacific that are then advected westward by the mean zonal current.

A natural question is whether a similar relationship with ENSO could occur with the NPMM. The mechanism described here requires that the WES feedback extends from the Southern Hemisphere into the Northern Hemisphere and whether the WES feedback associated with meridional modes extends into the opposite hemisphere depends on the background winds (Liu and Xie 1994; Wang 2010b; Okumura 2013; Zhang et al. 2014b). Using an atmosphere general circulation model coupled to a SOM, Zhang et al. (2014b) demonstrate that a meridional mode, whether originating in the Northern or Southern Hemisphere, can only expand into the opposite hemisphere if the ITCZ is located in the opposite hemisphere. This is primarily due to the meridional component of the winds (i.e., the winds the meridional mode would need to oppose to generate a LHF signal that extends across the equator) as shown in the analytic studies using simpler models by Liu and Xie (1994) and Wang (2010b). Since the NPMM exists in the same hemisphere as the observed ITCZ, the NPMM should not extend across the equator according to Zhang et al. (2014b) and therefore the mechanism presented in this study would not hold true for the NPMM. That said, even if the NPMM were to extend across the equator, it would do so in the western-central Pacific and not the eastern Pacific; therefore, in either case, we do not expect the argument presented in this study to be valid for the NPMM.

As for the forcing mechanism of the SPMM, Fig. 11 verifies that SPMM is linked to midlatitude atmospheric variability the previous austral fall, consistent with Zhang et al. (2014a) and Ding et al. (2015), and

evidently does not require any tropical forcing (absent in ClimWinds). The timing of the atmospheric forcing reflects Southern Hemisphere seasonality consistent with Jin and Kirtman (2009). The SPMM composite SLP anomaly pattern and the 500-hPa geopotential heights anomaly pattern exhibit similar structure in the Southern Hemisphere throughout the evolution, revealing that the forcing includes a barotropic component. Both the surface and midlevel expressions appear in March–May and strengthen simultaneously, reaching maximum strength in June–August. The pattern noticeably weakens in September, with the SST and LHF anomalies lagging by one month (Fig. 7). The surface and midlevel atmospheric structures are similar to those in Garreaud and Battisti (1999), who describe decadal eastern equatorial Pacific SST variability using observationally based fields. In fact, Garreaud and Battisti (1999) suggest that the forcing mechanism of the decadal SST variability could be from LHF anomalies associated with the anomalous circulation pattern. This interpretation is consistent with the SPMM results we show here.

The SPMM could impact ENSO in two ways in which LHF anomalies are important. First, if the SPMM is not correctly forecasted in seasonal climate predictions, then the SPMM may serve as a source of error in the coincident ENSO forecast. In other words, if the LHF signal in the Niño-3 region associated with the SPMM is different from what is seen in observations, the amplitude of the predicted coincident ENSO event could be wrong. Second, the SPMM variability superimposed onto ENSO variability, as seen in Fig. 2b, may actually be the decadal variability seen in prior studies. This hypothesis is different than in Di Lorenzo et al. (2015), in which the authors hypothesize that the combination of the NPMM and ENSO modes, and the associated tropical-to-extratropical and extratropical-to-tropic interactions, generates the decadal Pacific variability signal. The mechanism here, with similarities to the Garreaud and Battisti (1999) and Okumura (2013) hypotheses for Pacific decadal variability originating in the Southern Hemisphere, suggests two independent modes of variability such that when they are coincidentally in phase, the resulting ENSO behavior on long time scales could take on a decadal signal. This coincidence may also explain the atmosphere–ocean general circulation model results in Toniazzo (2010) showing that roughly 1/3 of ENSO events are linked to variability in the SE Pacific resembling the SPMM. As such, it is not surprising that the SPMM and Pacific decadal variability SSTA patterns in the literature are similar, as the SPMM may be the variability in tandem with ENSO generating the decadal signal. Moreover, since the SPMM is described as stochastically forced by extratropical atmospheric variability, it is no surprise that subtropical atmospheric noise has been shown to excite Pacific decadal variability (e.g., Yeh and Kirtman 2006), consistent with the proposed role of the SPMM in decadal variability described here. It is, of course, possible that meridional modes in both the Northern and Southern Hemispheres, in tandem with ENSO, contribute to the decadal variability (Yeh and Kirtman 2006).

Overall, the results in this study make a case for a thermally driven component in ENSO amplitude and uncertainty, in addition to the well-established wind-driven component. The mechanism proposed in the present study is distinctly different from the Zhang et al. (2014a) hypothesis that the SPMM remotely influences winds in the central Pacific that trigger ENSO events. Instead, we show here that the SPMM modulates ENSO amplitude by modulating the effectiveness of the LHF damping. Further assessment of whether climate prediction models like those of the North American Multi-Model Ensemble (Kirtman et al. 2014) prediction system accurately represent and predict SPMM at short lead times is of particular interest. A similar skill assessment of the SPMM as is done in Larson and Kirtman (2014) with the NPMM and Pegion and Alexander (2013) with the seasonal footprint mechanism may be a worthwhile next step to establish a baseline for expectations in incorporating the SPMM into further ENSO predictability and uncertainty discussions.

Acknowledgments. This research was supported by the NOAA Climate and Global Change Postdoctoral Fellowship Program sponsored by the NOAA Climate Program Office and administered by the University Corporation for Atmospheric Research Cooperative Programs for the Advancement of Earth System Science (CPAESS). The authors also acknowledge computational support from the University of Miami Center for Computational Science. The authors thank three anonymous reviewers for constructive comments that improved the manuscript.

REFERENCES

Alexander, M. A., D. J. Vimont, P. Chang, and J. D. Scott, 2010: The impact of extratropical atmospheric variability on ENSO: Testing the seasonal footprinting mechanism using coupled model experiments. *J. Climate*, **23**, 2885–2901, https://doi.org/10.1175/2010JCLI3205.1.

Anderson, B. T., 2007: On the joint role of subtropical atmospheric variability and equatorial subsurface heat content anomalies in initiating the onset of ENSO events. *J. Climate*, **20**, 1593–1599, https://doi.org/10.1175/JCLI4075.1.

——, and R. C. Perez, 2015: ENSO and non-ENSO induced charging and discharging of the equatorial Pacific.

Climate Dyn., **45**, 2309–2327, https://doi.org/10.1007/s00382-015-2472-x.

——, ——, and A. Karspeck, 2013: Triggering of El Niño onset through trade wind–induced charging of the equatorial Pacific. *Geophys. Res. Lett.*, **40**, 1212–1216, https://doi.org/10.1002/grl.50200.

Becker, E., and H. van den Dool, 2016: Probabilistic seasonal forecasts in the North American multimodel ensemble: A baseline skill assessment. *J. Climate*, **29**, 3015–3026, https://doi.org/10.1175/JCLI-D-14-00862.1.

Bellenger, H., E. Guilyardi, J. Leloup, M. Lengaigne, and J. Vialard, 2014: ENSO representation in climate models: From CMIP3 to CMIP5. *Climate Dyn.*, **42**, 1999–2018, https://doi.org/10.1007/s00382-013-1783-z.

Bitz, C. M., K. M. Shell, P. R. Gent, D. A. Bailey, G. Danabasoglu, K. C. Armour, M. M. Holland, and J. T. Kiehl, 2012: Climate sensitivity of the Community Climate System Model, version 4. *J. Climate*, **25**, 3053–3070, https://doi.org/10.1175/JCLI-D-11-00290.1.

Capotondi, A., 2013: ENSO diversity in the NCAR CCSM4 climate model. *J. Geophys. Res. Oceans*, **118**, 4755–4770, https://doi.org/10.1002/jgrc.20335.

Chang, P., L. Zhang, R. Saravanan, D. J. Vimont, J. C. H. Chiang, L. Ji, H. Seidel, and M. K. Tippett, 2007: Pacific meridional mode and El Niño–Southern Oscillation. *Geophys. Res. Lett.*, **34**, L16608, https://doi.org/10.1029/2007GL030302.

Chen, L.-C., H. van den Dool, E. Becker, and Q. Zhang, 2017: ENSO precipitation and temperature forecasts in the North American Multimodel Ensemble: Composite analysis and validation. *J. Climate*, **30**, 1103–1125, https://doi.org/10.1175/JCLI-D-15-0903.1.

Chen, X., and J. M. Wallace, 2015: ENSO-like variability: 1900–2013. *J. Climate*, **28**, 9623–9641, https://doi.org/10.1175/JCLI-D-15-0322.1.

Chiang, J. C. H., and D. J. Vimont, 2004: Analogous Pacific and Atlantic meridional modes of tropical atmosphere–ocean variability. *J. Climate*, **17**, 4143–4158, https://doi.org/10.1175/JCLI4953.1.

Clement, A., P. DiNezio, and C. Deser, 2011: Rethinking the ocean's role in the Southern Oscillation. *J. Climate*, **24**, 4056–4072, https://doi.org/10.1175/2011JCLI3973.1.

Deser, C., and Coauthors, 2012: ENSO and Pacific decadal variability in the Community Climate System Model version 4. *J. Climate*, **25**, 2622–2651, https://doi.org/10.1175/JCLI-D-11-00301.1.

Di Lorenzo, E., G. Liguori, N. Schneider, J. C. Furtado, B. T. Anderson, and M. A. Alexander, 2015: ENSO and meridional modes: A null hypothesis for Pacific climate variability. *Geophys. Res. Lett.*, **42**, 9440–9448, https://doi.org/10.1002/2015GL066281.

DiNezio, P. N., and C. Deser, 2014: Nonlinear controls on the persistence of La Niña. *J. Climate*, **27**, 7335–7355, https://doi.org/10.1175/JCLI-D-14-00033.1.

——, ——, Y. Okumura, and A. Karspeck, 2017: Predictability of 2-year La Niña events in a coupled general circulation model. *Climate Dyn.*, **49**, 4237–4261, https://doi.org/10.1007/s00382-017-3575-3.

Ding, R., J. Li, and Y.-H. Tseng, 2015: The impact of South Pacific extratropical forcing on ENSO and comparisons with the North Pacific. *Climate Dyn.*, **44**, 2017–2034, https://doi.org/10.1007/s00382-014-2303-5.

Doblas-Reyes, F. J., M. Déqué, and J.-P. Piedelievre, 2000: Multi-model spread and probabilistic seasonal forecasts in PROVOST. *Quart. J. Roy. Meteor. Soc.*, **126**, 2069–2087, https://doi.org/10.1002/qj.49712656705.

Eisenman, I., L. Yu, and E. Tziperman, 2005: Westerly wind bursts: ENSO's tail rather than the dog? *J. Climate*, **18**, 5224–5238, https://doi.org/10.1175/JCLI3588.1.

Fedorov, A. V., 2002: The response of the coupled tropical ocean–atmosphere to westerly wind bursts. *Quart. J. Roy. Meteor. Soc.*, **128**, 1–23, https://doi.org/10.1002/qj.200212857901.

Garreaud, R. D., and D. S. Battisti, 1999: Interannual (ENSO) and interdecadal (ENSO-like) variability in the Southern Hemisphere tropospheric circulation. *J. Climate*, **12**, 2113–2123, https://doi.org/10.1175/1520-0442(1999)012<2113:IEAIEL>2.0.CO;2.

Gebbie, G., I. Eisenman, A. Wittenberg, and E. Tziperman, 2007: Modulation of westerly wind bursts by sea surface temperature: A semistochastic feedback for ENSO. *J. Atmos. Sci.*, **64**, 3281–3295, https://doi.org/10.1175/JAS4029.1.

Gent, P. R., and Coauthors, 2011: The Community Climate System Model version 4. *J. Climate*, **24**, 4973–4991, https://doi.org/10.1175/2011JCLI4083.1.

Giese, B. S., and D. E. Harrison, 1991: Eastern equatorial Pacific response to three composite westerly wind types. *J. Geophys. Res.*, **96**, 3239–3248, https://doi.org/10.1029/90JC01861.

Guilyardi, E., A. Wittenberg, A. Fedorov, M. Collins, C. Wang, A. Capotondi, G. J. Van Oldenborgh, and T. Stockdale, 2009: Understanding El Niño in ocean–atmosphere general circulation models: Progress and challenges. *Bull. Amer. Meteor. Soc.*, **90**, 325–340, https://doi.org/10.1175/2008BAMS2387.1.

Harrison, D. E., and G. A. Vecchi, 1997: Westerly wind events in the tropical Pacific, 1986–95. *J. Climate*, **10**, 3131–3156, https://doi.org/10.1175/1520-0442(1997)010<3131:WWEITT>2.0.CO;2.

Hu, S., and A. V. Fedorov, 2018: The extreme El Niño of 2015–2016: The role of westerly and easterly wind bursts, and preconditioning by the failed 2014 event. *Climate Dyn.*, https://doi.org/10.1007/s00382-017-3531-2, in press.

Infanti, J. M., and B. P. Kirtman, 2016: North American rainfall and temperature prediction response to the diversity of ENSO. *Climate Dyn.*, **46**, 3007–3023, https://doi.org/10.1007/s00382-015-2749-0.

Jin, D., and B. P. Kirtman, 2009: Why the Southern Hemisphere ENSO responses lead ENSO. *J. Geophys. Res.*, **114**, D23101, https://doi.org/10.1029/2009JD012657.

Jin, F.-F., 1997: An equatorial recharge paradigm for ENSO. Part I: Conceptual model. *J. Atmos. Sci.*, **54**, 811–829, https://doi.org/10.1175/1520-0469(1997)054<0811:AEORPF>2.0.CO;2.

Karspeck, A. R., A. Kaplan, and M. A. Cane, 2006: Predictability loss in an intermediate ENSO model due to initial error and atmospheric noise. *J. Climate*, **19**, 3572–3588, https://doi.org/10.1175/JCLI3818.1.

Kessler, W. S., L. M. Rothstein, and D. Chen, 1998: The annual cycle of SST in the eastern tropical Pacific, diagnosed in an ocean GCM. *J. Climate*, **11**, 777–799, https://doi.org/10.1175/1520-0442(1998)011<0777:TACOSI>2.0.CO;2.

Kirtman, B. P., and Coauthors, 2014: The North American Multimodel Ensemble: Phase-1 seasonal-to-interannual prediction; phase-2 toward developing intraseasonal prediction. *Bull. Amer. Meteor. Soc.*, **95**, 585–601, https://doi.org/10.1175/BAMS-D-12-00050.1.

Kleeman, R., and A. M. Moore, 1997: A theory for the limitation of ENSO predictability due to stochastic atmospheric transients. *J. Atmos. Sci.*, **54**, 753–767, https://doi.org/10.1175/1520-0469(1997)054<0753:ATFTLO>2.0.CO;2.

——, and ——, 1999: A new method for determining the reliability of dynamical ENSO predictions. *Mon. Wea. Rev.*, **127**, 694–705, https://doi.org/10.1175/1520-0493(1999)127<0694:ANMFDT>2.0.CO;2.

Larson, S. M., and B. P. Kirtman, 2013: The Pacific meridional mode as a trigger for ENSO in a high resolution coupled model. *Geophys. Res. Lett.*, **40**, 3189–3194, https://doi.org/10.1002/grl.50571.

——, and ——, 2014: The Pacific meridional mode as an ENSO precursor and predictor in the North American multi-model ensemble. *J. Climate*, **27**, 7018–7032, https://doi.org/10.1175/JCLI-D-14-00055.1.

——, and ——, 2015a: An alternate approach to ensemble ENSO forecast spread: Application to the 2014 forecast. *Geophys. Res. Lett.*, **42**, 9411–9415, https://doi.org/10.1002/2015GL066173.

——, and ——, 2015b: Revisiting ENSO coupled instability theory and SST error growth in a fully coupled model. *J. Climate*, **28**, 4724–4742, https://doi.org/10.1175/JCLI-D-14-00731.1.

——, and ——, 2017: Drivers of coupled model ENSO error dynamics and the spring predictability barrier. *Climate Dyn.*, **48**, 3631–3644, https://doi.org/10.1007/s00382-016-3290-5.

——, and ——, 2018: Linking preconditioning to extreme ENSO events and reduced ensemble spread. *Climate Dyn.*, https://doi.org/10.1007/s00382-017-3791-x, in press.

——, ——, and D. J. Vimont, 2017: A framework to decompose wind-driven biases in climate models applied to CCSM/CESM in the eastern Pacific. *J. Climate*, **30**, 8763–8782, https://doi.org/10.1175/JCLI-D-17-0099.1.

——, D. J. Vimont, A. C. Clement, and B. P. Kirtman, 2018: How momentum coupling affects SST variance and large-scale Pacific climate variability in CESM. *J. Climate*, **31**, 3927–3944, https://doi.org/10.1175/JCLI-D-17-0645.1.

Lengaigne, M., J.-P. Boulanger, C. Menkes, S. Masson, G. Madec, and P. Delecluse, 2002: Ocean response to the March 1997 westerly wind event. *J. Geophys. Res.*, **107**, 8015, https://doi.org/10.1029/2001JC000841.

Levine, A. F. Z., and M. J. McPhaden, 2016: How the July 2014 easterly wind burst gave the 2015–2016 El Niño a head start. *Geophys. Res. Lett.*, **43**, 6503–6510, https://doi.org/10.1002/2016GL069204.

Liu, Z., and S. Xie, 1994: Equatorward propagation of coupled air–sea disturbances with application to the annual cycle of the eastern tropical Pacific. *J. Atmos. Sci.*, **51**, 3807–3822, https://doi.org/10.1175/1520-0469(1994)051<3807:EPOCAD>2.0.CO;2.

Lopez, H., and B. P. Kirtman, 2013: Westerly wind bursts and the diversity of ENSO in CCSM3 and CCSM4. *Geophys. Res. Lett.*, **40**, 4722–4727, https://doi.org/10.1002/grl.50913.

——, ——, E. Tziperman, and G. Gebbie, 2013: Impact of interactive westerly wind bursts on CCSM3. *Dyn. Atmos. Oceans*, **59**, 24–51, https://doi.org/10.1016/j.dynatmoce.2012.11.001.

Luther, D. S., D. E. Harrison, and R. A. Knox, 1983: Zonal winds in the central equatorial Pacific and El Niño. *Science*, **222**, 327–331, https://doi.org/10.1126/science.222.4621.327.

Ma, J., S.-P. Xie, and H. Xu, 2017: Contributions of the North Pacific meridional mode to ensemble spread of ENSO prediction. *J. Climate*, **30**, 9167–9181, https://doi.org/10.1175/JCLI-D-17-0182.1.

McPhaden, M. J., 2003: Tropical Pacific Ocean heat content variations and ENSO persistence barriers. *Geophys. Res. Lett.*, **30**, 1480, https://doi.org/10.1029/2003GL016872.

——, and X. Yu, 1999: Equatorial waves and the 1997–98 El Niño. *Geophys. Res. Lett.*, **26**, 2961–2964, https://doi.org/10.1029/1999GL004901.

——, F. Bahr, Y. Du Penhoat, E. Firing, S. P. Hayes, P. P. Niiler, P. L. Richardson, and J. M. Toole, 1992: The response of the western equatorial Pacific Ocean to westerly wind bursts during November 1989 to January 1990. *J. Geophys. Res.*, **97**, 14 289–14 303, https://doi.org/10.1029/92JC01197.

Menkes, C. E., M. Lengaigne, J. Vialard, M. Puy, P. Marchesiello, S. Cravatte, and G. Cambon, 2014: About the role of westerly wind events in the possible development of an El Niño in 2014. *Geophys. Res. Lett.*, **41**, 6476–6483, https://doi.org/10.1002/2014GL061186.

Min, Q., J. Su, and R. Zhang, 2017: Impact of the South and North Pacific meridional modes on the El Niño–Southern Oscillation: Observational analysis and comparison. *J. Climate*, **30**, 1705–1720, https://doi.org/10.1175/JCLI-D-16-0063.1.

Mo, K. C., and J. E. Schemm, 2008: Relationships between ENSO and drought over the southeastern United States. *Geophys. Res. Lett.*, **35**, L15701, https://doi.org/10.1029/2008GL034656.

Moore, A. M., and R. Kleeman, 1999: Stochastic forcing of ENSO by the intraseasonal oscillation. *J. Climate*, **12**, 1199–1220, https://doi.org/10.1175/1520-0442(1999)012<1199:SFOEBT>2.0.CO;2.

Moum, J. N., R.-C. Lien, A. Perlin, J. D. Nash, M. C. Gregg, and P. J. Wiles, 2009: Sea surface cooling at the equator by subsurface mixing in tropical instability waves. *Nat. Geosci.*, **2**, 761–765, https://doi.org/10.1038/ngeo657.

Okumura, Y. M., 2013: Origins of tropical Pacific decadal variability: Role of stochastic atmospheric forcing from the South Pacific. *J. Climate*, **26**, 9791–9796, https://doi.org/10.1175/JCLI-D-13-00448.1.

Palmer, T. N., and Coauthors, 2004: Development of a European Multimodel Ensemble System for Seasonal-to-Interannual Prediction (DEMETER). *Bull. Amer. Meteor. Soc.*, **85**, 853–872, https://doi.org/10.1175/BAMS-85-6-853.

Pegion, K., and M. Alexander, 2013: The seasonal footprinting mechanism in CFSv2: Simulation and impact on ENSO prediction. *Climate Dyn.*, **41**, 1671–1683, https://doi.org/10.1007/s00382-013-1887-5.

——, and C. Selman, 2017: Extratropical precursors of the El Niño–Southern Oscillation. *Climate Extremes: Patterns and Mechanisms*, *Geophys. Monogr.*, Vol. 226, Amer. Geophys. Union, 299–314.

Peng, P., A. Kumar, M. S. Halpert, and A. G. Barnston, 2012: An analysis of CPC's operational 0.5-month lead seasonal outlooks. *Wea. Forecasting*, **27**, 898–917, https://doi.org/10.1175/WAF-D-11-00143.1.

Perez, R. C., R. Lumpkin, W. E. Johns, G. R. Foltz, and V. Hormann, 2012: Interannual variations of Atlantic tropical instability waves. *J. Geophys. Res.*, **117**, C03011, https://doi.org/10.1029/2011JC007584.

Picaut, J., and T. Delcroix, 1995: Equatorial wave sequence associated with warm pool displacements during the 1986–1989 El Niño-La Niña. *J. Geophys. Res.*, **100**, 18393–18408, https://doi.org/10.1029/95JC01358.

Puy, M., J. Vialard, M. Lengaigne, and E. Guilyardi, 2016: Modulation of equatorial Pacific westerly/easterly wind events by the Madden–Julian oscillation and convectively-coupled Rossby waves. *Climate Dyn.*, **46**, 2155–2178, https://doi.org/10.1007/s00382-015-2695-x.

Samelson, R. M., and E. Tziperman, 2001: Instability of the chaotic ENSO: The growth-phase predictability barrier. *J. Atmos. Sci.*, **58**, 3613–3625, https://doi.org/10.1175/1520-0469(2001)058<3613:IOTCET>2.0.CO;2.

Thomas, E. E., and D. J. Vimont, 2016: Modeling the mechanisms of linear and nonlinear ENSO responses to the Pacific

meridional mode. *J. Climate*, **29**, 8745–8761, https://doi.org/10.1175/JCLI-D-16-0090.1.

Toniazzo, T., 2010: Climate variability in the south-eastern tropical Pacific and its relation with ENSO: A GCM study. *Climate Dyn.*, **34**, 1093–1114, https://doi.org/10.1007/s00382-009-0602-z.

Trenberth, K. E., and J. W. Hurrell, 1994: Decadal atmosphere–ocean variations in the Pacific. *Climate Dyn.*, **9**, 303–319, https://doi.org/10.1007/BF00204745.

Tziperman, E., and L. Yu, 2007: Quantifying the dependence of westerly wind bursts on the large-scale tropical Pacific SST. *J. Climate*, **20**, 2760–2768, https://doi.org/10.1175/JCLI4138a.1.

Vimont, D. J., 2005: The contribution of the interannual ENSO cycle to the spatial pattern of decadal ENSO-like variability. *J. Climate*, **18**, 2080–2092, https://doi.org/10.1175/JCLI3365.1.

——, 2010: Transient growth of thermodynamically coupled variations in the tropics under an equatorially symmetric mean state. *J. Climate*, **23**, 5771–5789, https://doi.org/10.1175/2010JCLI3532.1.

——, D. S. Battisti, and A. C. Hirst, 2003a: The seasonal footprinting mechanism in the CSIRO general circulation models. *J. Climate*, **16**, 2653–2667, https://doi.org/10.1175/1520-0442(2003)016<2653:TSFMIT>2.0.CO;2.

——, J. M. Wallace, and D. S. Battisti, 2003b: The seasonal footprinting mechanism in the Pacific: Implications for ENSO. *J. Climate*, **16**, 2668–2675, https://doi.org/10.1175/1520-0442(2003)016<2668:TSFMIT>2.0.CO;2.

Wang, F., 2010a: Subtropical dipole mode in the Southern Hemisphere: A global view. *Geophys. Res. Lett.*, **37**, L10702, https://doi.org/10.1029/2010GL042750.

——, 2010b: Thermodynamic coupled modes in the tropical atmosphere–ocean: An analytical solution. *J. Atmos. Sci.*, **67**, 1667–1677, https://doi.org/10.1175/2009JAS3262.1.

Xue, Y., M. A. Cane, and S. E. Zebiak, 1997: Predictability of a coupled model of ENSO using singular vector analysis. Part I: Optimal growth in seasonal background and ENSO cycles. *Mon. Wea. Rev.*, **125**, 2043–2056, https://doi.org/10.1175/1520-0493(1997)125<2043:POACMO>2.0.CO;2.

Yeh, S.-W., and B. P. Kirtman, 2004: Tropical Pacific decadal variability and ENSO amplitude modulation in a CGCM. *J. Geophys. Res.*, **109**, C11009, https://doi.org/10.1029/2004JC002442.

——, and ——, 2006: Origin of decadal El Niño–Southern Oscillation–like variability in a coupled general circulation model. *J. Geophys. Res.*, **111**, C01009, https://doi.org/10.1029/2005JC002985.

You, Y., and J. C. Furtado, 2017: The role of South Pacific atmospheric variability in the development of different types of ENSO. *Geophys. Res. Lett.*, **44**, 7438–7446, https://doi.org/10.1002/2017GL073475.

Zhang, H., A. Clement, and P. DiNezio, 2014a: The South Pacific meridional mode: A mechanism for ENSO-like variability. *J. Climate*, **27**, 769–783, https://doi.org/10.1175/JCLI-D-13-00082.1.

——, C. Deser, A. Clement, and R. Tomas, 2014b: Equatorial signatures of the Pacific meridional modes: Dependence on mean climate state. *Geophys. Res. Lett.*, **41**, 568–574, https://doi.org/10.1002/2013GL058842.

Zhang, Y., J. M. Wallace, and D. S. Battisti, 1997: ENSO-like interdecadal variability: 1900–93. *J. Climate*, **10**, 1004–1020, https://doi.org/10.1175/1520-0442(1997)010<1004:ELIV>2.0.CO;2.